Enhanced osteochondral regeneration with a 3D-Printed biomimetic scaffold featuring a calcified interfacial layer

Di Wu [a,1], Kaiwen Zheng [a,1], Wenjing Yin [a,1], Bin Hu [b], Mingzhao Yu [a], Qingxiao Yu [c], Xiaojuan Wei [b,*], Jue Deng [d,**], Changqing Zhang [a,***]

[a] *Department of Orthopedic Surgery, Shanghai Sixth People's Hospital Affiliated to Shanghai Jiao Tong University School of Medicine, No.600 Yishan Road, Shanghai, 200233, China*
[b] *Institute of Microsurgery on Extremities, Shanghai Sixth People's Hospital Affiliated to Shanghai Jiao Tong University School of Medicine, No.600 Yishan Road, Shanghai, 200233, China*
[c] *Shanghai Uniorlechnology Corporation, No. 258 Xinzhuan Road, Shanghai, 201612, China*
[d] *Academy for Engineering & Technology, Fudan University, No. 220 Handan Road, Shanghai, 200433, China*

ARTICLE INFO

ABSTRACT

The integrative regeneration of both articular cartilage and subchondral bone remains an unmet clinical need due to the difficulties of mimicking spatial complexity in native osteochondral tissues for artificial implants. Layer-by-layer fabrication strategies, such as 3D printing, have emerged as a promising technology replicating the stratified zonal architecture and varying microstructures and mechanical properties. However, the dynamic and circulating physiological environments, such as mass transportation or cell migration, usually distort the pre-confined biological properties in the layered implants, leading to undistinguished spatial variations and subsequently inefficient regenerations. This study introduced a biomimetic calcified interfacial layer into the scaffold as a compact barrier between a cartilage layer and a subchondral bone layer to facilitate osteogenic–chondrogenic repair. The calcified interfacial layer consisting of compact polycaprolactone (PCL), nano-hydroxyapatite, and tasquinimod (TA) can physically and biologically separate the cartilage layer (TA-mixed, chondrocytes-load gelatin methacrylate) from the subchondral bond layer (porous PCL). This introduction preserved the as-designed independent biological environment in each layer for both cartilage and bone regeneration, successfully inhibiting vascular invasion into the cartilage layer and preventing hyaluronic cartilage calcification owing to devascularization of TA. The improved integrative regeneration of cartilage and subchondral bone was validated through gross examination, micro-computed tomography (micro-CT), and histological and immunohistochemical analyses based on an *in vivo* rat model. Moreover, gene and protein expression studies identified a key role of Caveolin (CAV-1) in promoting angiogenesis through the Wnt/β-catenin pathway and indicated that TA in the calcified layer blocked angiogenesis by inhibiting CAV-1.

1. Introduction

The management of osteochondral lesions has been a clinical challenge for over a century [1], affecting millions of individuals globally due to injury, disease, or aging. Although articular cartilage and subchondral bone are anatomically proximate, they significantly diverge in terms of three-dimensional tissue morphologies, mechanical properties, and biological functions [2] (Fig. 1a). For example, the cartilage tissues lack vasculature and lymphatic structures. They are soft and robust in mechanics, and mature chondrocytes have limited proliferation and migration capabilities. In contrast, the subchondral bones are strong, possess vasculature and lymphatic structures, and are conducive to proliferation and migration. This divergence makes the integrative repair of osteochondral defects particularly challenging. Also, inefficient

repair often results in instability, pain, and impaired functionality. Current clinical surgical treatments, including microfracture, autologous stem cell/chondrocyte transplantation, and even arthroplasty, have been proposed for repairing such defects [3,4]. However, these methods have limitations, such as graft deterioration/lack of integration, mechanically insufficient cartilage formation, and donor site morbidity, contributing to unsatisfactory patient outcomes. Moreover, these treatments primarily focus on repairing the articular cartilage tissue, potentially resulting in the formation of fibrocartilage or poor integration with the subchondral bone [5,6].

The development of tissue scaffolds that replicate both the structural and functional characteristics of native tissue is an emerging strategy for osteochondral repair [7–9]. One promising method is multi-material 3D bioprinting technology, which enables the recreation of the stratified zonal architecture through layer-by-layer manufacturing [10–12]. The depth-dependent porosity, stiffness, and geometry can be easily adjusted in the 3D-printed scaffold [13]. Furthermore, incorporating living cells and bioactive materials into different zones of the scaffold offers distinct microenvironments that promote chondrogenic and osteogenic regeneration [14–16]. However, when these layered scaffolds are exposed to dynamic and circulating physiological environments, the clear distinction between different layers tends to blur over time, primarily due to mass diffusion and/or cell migration. Consequently, the biological properties of different zones in traditional scaffolds become unified, ultimately reducing the efficiency of osteochondral regeneration, such as heterotopic ossification (Fig. 1b). In contrast, a calcified interfacial layer exists between the native cartilage and the subchondral bone in the nature (Fig. 1a) [17]. This layer acts as a barrier, inhibiting vascular invasion into the cartilage and preventing the calcification of hyaluronic cartilage. Engineering a calcified interfacial layer in the 3D-printed scaffold, inspired by this natural physiological structure, emerges as a promising, yet often overlooked, solution [18,19]. Introducing such a layer makes it possible to restore osteochondral tissues with both functional and structural properties and gain a deeper understanding of the underlying biological mechanisms involved.

Tasquinimod (TA) exerts an anti-angiogenic effect by down-regulating hypoxia-inducible factor-1α (HIF-1α) and vascular endothelial growth factor (VEGF), inducing the upregulation of thrombospondin-1 [20]. Jin et al. revealed that TA inhibited endothelial cell proliferation, migration, and lumen formation [21]. The present study first used TA to inhibit vascular regeneration in cartilage repair. TA, as a small-molecule drug, was mixed into the bioinks of the cartilage layer and calcified interfacial layer to inhibit neovascularization. Hydroxyapatite (HA) has also been widely studied for bone tissue engineering applications due to its good mechanical strength and similarity to the mineralized areas of native bone tissue; it is designed as an important component of the calcified interfacial layer [22]. PCL, a Food and Drug Administration–approved synthetic biodegradable polymer, has been widely used for biomedical applications. Many studies have described the development of PCL scaffolds by additive manufacturing owing to their well-assessed melt processing, osteoinductive, and mechanical properties [23]. A PCL-HA composite material demonstrated enhanced osteogenic ability in bone repair [24]. Gelatin methacrylate (GelMA), an ideal photo-crosslinking gelatin-based hydrogel, has been used as a cartilage-regenerating scaffold owing to its biocompatibility and biomimetic properties [25–27]. Furthermore, gelatin-based hydrogels can provide sustained release of growth factors as well as promote cell attachment and cell differentiation toward cartilage-like tissues [28, 29].

In this study, we introduced a biomimetic calcified layer into our scaffold, serving as a compact interface between the top and bottom layers, to facilitate osteogenic–chondrogenic repair. The calcified interfacial layer was composed of compact polycaprolactone (PCL), nano-hydroxyapatite (nHA), and TA, effectively physically and functionally separating the top layer (GelMA with chondrocytes loaded and mixed with TA for cartilage repair) from the bottom layer (porous PCL for subchondral bone repair) (Fig. 1c). The invasion of regenerated cartilage tissue toward the subchondral bone and the vascularization of hyaline cartilage were blocked by the biomimetic calcified layer, which also acted as a compact barrier (Fig. 1d). The incorporation of the calcified interfacial layer preserved the distinct biological environments in each layer, enabling independent cartilage and bone regeneration. It successfully inhibited vascular invasion into the top layer and prevented the calcification of hyaluronic cartilage (Fig. 1e). We conducted thorough assessments to validate the improved integrative regeneration of both cartilage and subchondral bone, including gross examination,
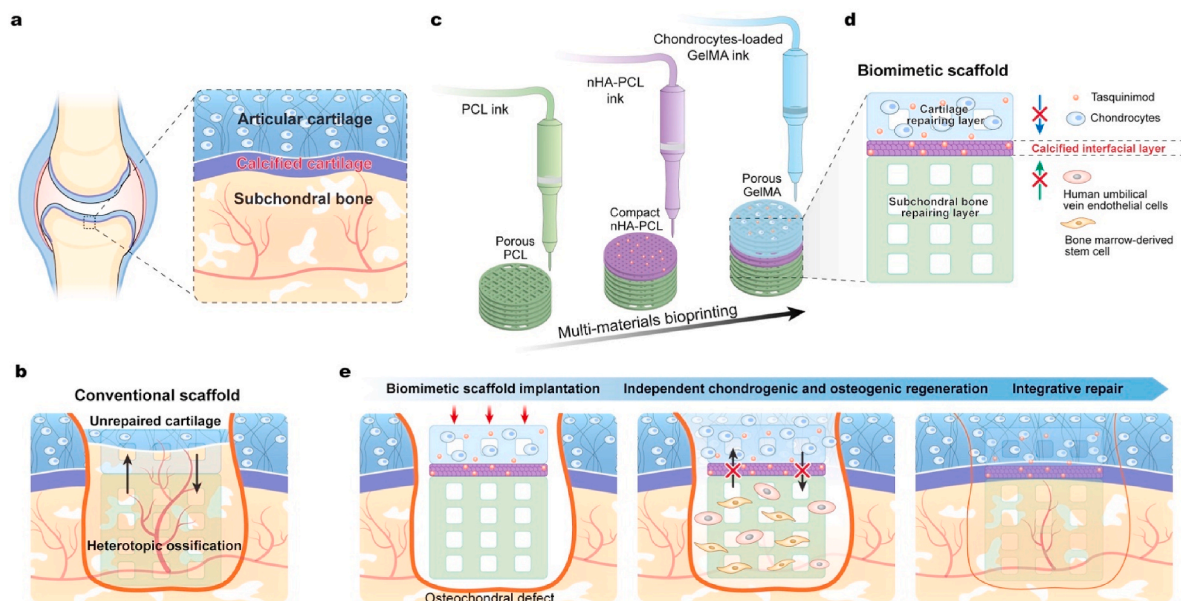
Fig. 1. Concept of 3D printed biomimetic scaffold. (a) Schematic illustration of native cartilage with the calcified interfacial layer between the articular cartilage and the subchondral bone; (b) Reduced efficiency of cartilage regeneration for the conventional scaffold due to the lack of a calcified interfacial layer; (c) Multi-materials bioprinting of biomimetic scaffold; (d) Cross-section of biomimetic scaffold showing the calcified interfacial layer; (e) Schematic illustration for integrative repair of the biomimetic scaffold in layer-specific chondrogenic and osteogenic induction and regeneration.

micro-computed tomography (micro-CT), and histological and immu-nohistochemical analyses, using an *in vivo* rat model. Furthermore, our gene and protein expression studies identified a crucial role played by CAV-1 in promoting angiogenesis through the Wnt/β-catenin pathway. Importantly, our findings indicated that TA in the interfacial calcified layer effectively blocked angiogenesis by inhibiting CAV-1, highlighting its significant contribution to the overall success of our approach.

2. Materials and methods

2.1. Cells and materials

Rat bone marrow–derived mesenchymal stem cells (BMSCs) and human umbilical vein endothelial cells (HUVECs) were obtained from ATCC (USA) and their culture conditions were previously described [30]. Phosphate-buffered saline (PBS), Dulbecco's modified Eagle's medium (DMEM), fetal bovine serum (FBS), and live/dead viability kit were purchased from Thermo Fisher Scientific. Needles were purchased from BD Biosciences (USA). TA (Selleck, USA) was dissolved in dimethyl sulfoxide (DMSO; Sigma–Aldrich, Shanghai, China) and stored at −20 °C. GelMA, gelatin, and PCL were purchased from SunP Biotech (Beijing, China). Primary antibodies of anti-COL-I, COL-II, Runx2, OCN, VEGF, CAV-1, β-catenin, GSK-3β, and *p*-GSK-3β were purchased from Abcam (Cambridge, UK). Gelatin (A type, derived from porcine skin), photoinitiator (PI, purity: 98%), alcian blue, and Alizarin Red S (ARS) were purchased from Sigma–Aldrich. Methacrylic anhydride (MA) was supplied by Shanghai Macklin Bio-Chem Technology Co., Ltd. (China). nHA was purchased from Shanghai Aladdin Bio-Chem Technology Co., Ltd. (China).

2.2. Fabrication of the printable scaffolds

2.2.1. Synthesis of GelMA

GelMA was synthesized by a previously described method [31]. Briefly, a 10% *w/v* solution of gelatin in deionized water was mixed with MA in a 1:0.6 (*v/v*) ratio at 50 °C for 3 h. MA was added to the gelatin solution at a rate of 0.5 mL/min under stirring conditions. The reaction was terminated by adding a sufficient amount of deionized water. The resulting solution was dialyzed in dialysis tubes (8–14 kDa) against ul-trapure water at 40 °C for 1 week to remove excess MA. Finally, the GelMA solution was filtered, freeze-dried, and stored at room temper-ature for further use. The GelMA solution was then combined with the photoinitiator. Subsequently, the solution was heated at 37 °C in a water bath, followed by sterilization using a 0.22-μm filter and then stored at 4 °C.

2.2.2. Chondrocyte-loaded GelMA hydrogel bioink preparation

Primary rat chondrocytes were isolated from femoral heads and condyles of Sprague–Dawley (SD) rats weighing 100 g. The cartilage fragments were minced and digested with 0.2% type II collagenase at 37 °C for 4 h. The cells were then resuspended in DMEM containing 10% FBS. When cells reached 80%–90% confluence, they were passaged using 0.25% trypsin digestion. All cells used were P2–P5 and maintained in a humidified incubator containing 5% CO_2 at 37 °C.

The lyophilized GelMA was dissolved in DMEM to obtain 5%, 10%, and 15% (*w/v*) GelMA hydrogels including 0.01 wt% PI. Primary rat chondrocytes were incorporated into GelMA at a density of 2×10^6 cells/mL before scaffold bioprinting. Crosslinking was accomplished by UV irradiation for 10 s (λ = 405 nm). All operations were performed in a sterile environment.

2.2.3. Synthesis of polycaprolactone nano-hydroxyapatite

For PCL-nHA composite synthesis, PCL (average molecular weight = 45,000 g/mol) and 3 wt% nHA (20 nm, purity ≥99%) were mixed in

dichloromethane at a ratio of 9:1. After partially volatilizing dichloro-methane, the obtained composites were 3D-printed into a compact scaffold using a fused deposition modeling (FDM) 3D printer. Before printing, PCL was adequately melted to ensure a smooth printing pro-cess, and a simple PCL was melted as a control. A 27G needle with an inner diameter of 200 μm was used.

2.2.4. 3D-printed biomimetic scaffolds

The biomimetic scaffold design pattern was set to three layers and bioprinted continuously (Supplementary Video). The modeling files (stl.) were input into the 3D bioprinter (Biomaker 2i; SunP Biotech) equipped with software for planning the printing path. On the printing platform at 21 °C, one nozzle was used for fused deposition of PCL at 70 °C, and the other nozzle was used to extrude chondrocyte-GelMA bioink at 21 °C. The first step was to print the bottom layer using PCL. Second, PCL, nHA, and TA were mixed and used to print the middle layer/calcified interfacial layer in a compact printing mode. Finally, chondrocytes-GelMA hydrogel mixed with TA was used to coat the top of the biomimetic scaffold. The biomimetic scaffold size was set as a cylinder with a 2 mm diameter and 1.5 mm thickness. Specifically, the PCL printed layer was set with a height of 1.0 mm (10 layers), the PCL-HA printed layer was set with a height of 0.2 mm (2 layers), and the chondrocytes-GelMA hydrogel layer was set with a thickness of 0.3 mm (3 layers). Specific printing conditions are listed in Table S1. Then, the scaffolds were photopolymerized in ultraviolet mold chambers (XL-1000 UV Crosslinker; Spectronics Corporation, NY, USA) at 3 mW/cm^2 for 1 min to ensure crosslinking.

2.3. Characterization of the composite scaffolds

2.3.1. ^1H NMR spectra and structural analysis

Gelatin and different concentrations of GelMA hydrogels (0.01 g) were dissolved in 0.55 mL of D_2O, and the ^1H NMR spectra of the samples were analyzed using an AVANCE III 400 spectrometer (Bruker, WI, USA). The Fourier-transform infrared spectroscopy (FTIR) analysis was conducted on a Fourier-transform infrared spectrometer (Bruker, WI, USA) to perform structural analysis, and the scan was performed from 600 to 4000 cm^{-1}.

2.3.2. Viscosity measurements and mechanical testing

A rotary rheometer (Malvern Instruments, Worcestershire, UK) with a 4° cone and plate geometry was used to determine the viscous behavior of GelMA (5%, 10%, and 15%) solutions. Viscosity was measured for increasing shear rates between 0.01 and 1000 s^{-1} at 25 °C. The compressive mechanical properties of the GelMA hydrogels (*n* = 4) were evaluated by performing compression tests. Cylindrical samples with a uniform shape (diameter: 10 mm, height: 2 mm) were prepared and tested to reduce measurement error. The cylindrical samples were immersed in PBS from their preparation. A strain rate of 0.1 mm/min was applied to the tested samples using a universal testing machine (Zwick Z020, Germany). The compressive Young's modulus was calcu-lated from the slope of the stress–strain curve in the linear regions.

2.3.3. Immersion experiments

The crosslinked GelMA hydrogels were immersed in a PBS solution at room temperature for 24 h to assess the water absorption. Excess surface water was removed with filter paper, and different concentrations of GelMA were weighed and recorded as wet weight. The samples were then lyophilized, weighed, and recorded as dry weight.

$$\text{Water absorption} = \frac{\text{Wet weight} - \text{Dry weight}}{\text{Dry weight}}$$

The degradation behaviors of GelMA were evaluated by the im-mersion test in simulated body fluid (SBF). The pH value of the SBF

solution was adjusted to 7.4 ± 0.1, and the samples were weighed daily to record weight losses. The degradation ratio was calculated as the dry weight ratio to the original dry weight at each time point. Each experiment contained four replicates.

$$Degradation\ ratio\ (\%) = \left(\frac{Original\ dry\ weight\ -\ Dry\ weight\ after\ degradation}{Original\ dry\ weight} \right) \times 100\%$$

2.3.4. Morphological observations

The samples were smeared on a cover glass, air-dried, and coated twice with palladium–platinum alloy at 40 mA. The surface morphology and details of the scaffolds were characterized using a scanning electron microscope (Hitachi, Tokyo, Japan). The surface morphologies of the nHA particles were characterized using a transmission electron microscope (Hitachi).

2.4. In vitro biocompatibility tests

2.4.1. TA drug screening

1 mg TA powder (S7617; Selleck, TX, USA) was first soaked in DMSO (10 nM) with shaking at 37 °C for 24 h, and the concentrations of TA in the medium were then diluted to 100, 10, 2, 1, and 0.1 μg/mL in sequence. The proliferation of chondrocytes was measured using the cell counting kit-8 (CCK-8; Dojindo, Tokyo, Japan) assay. The chondrocytes (5×10^3 cells/well) were seeded in the medium containing various concentrations of TA (100, 10, 2, 1, 0.1 and 0 μg/mL) using 96-well plates (each group: $n = 4$). After culturing for 1, 3, 5, and 7 days, the CCK-8 reagent was added to the medium, and the absorbance at 450 nm was measured 2 h later. Similarly, HUVECs were co-cultured with different concentrations of TA for determining the cell survival rate.

2.4.2. Cell viability

The survival rate was assessed following the manufacturer's protocol (LIVE/DEAD viability/cytotoxicity kit; Invitrogen, CA, USA) to quantify chondrocyte viability after incorporating into different concentrations of GelMA. A confocal laser scanning microscope (Leica SD AF, Leica, amburg, Germany) was used, in which the living cells were stained green using calcein with excitation at 488 nm, whereas the dead cells were stained red using EthD-1 with excitation at 561 nm. Five images were randomly captured within the cell-laden scaffolds and collected for quantitative analysis. Live and dead cells were counted automatically using Image-Pro Plus 6.0 software on days 1, 3, and 7.

2.4.3. Drug-loaded release of materials

A key test for assessing the performance of TA-loaded materials is quantifying its drug release capacities. Briefly, GelMA scaffold and PCL-HA scaffold loaded with tasquinimod (10 μmol) were respectively placed in 10 mL PBS and allowed to release for 14 days. Every 2 days, 100 μL of the solution from each group were drawn with a pipette, added to a 96-well plate, and 100 μL of PBS were added immediately after extraction to supplement the experimental solution. Results were quantified using a microplate reader ($n = 3$).

2.4.4. Chondrogenesis tests

For the chondrogenesis tests, the chondrocytes-incorporating hydrogels were incubated in chondrogenic induction medium (normal medium supplemented with 40 ng/mL of dexamethasone, 50 mg/mL of ascorbic acid, 6 mg/mL of insulin–transferrin–selenium premix, 1 mM sodium pyruvate, and 0.4 mM proline) (Sigma–Aldrich, MO, USA). Chondrogenesis was assessed by alcian blue staining to verify the efficacy, in which enhanced proteoglycan staining of chondrocytes indicated a positive result.

2.4.5. Osteogenesis tests

The osteogenic differentiation of BMSCs was initiated 24 h after the incubation of scaffold extracts. Briefly, the original medium was replaced with an osteogenic differentiation medium (HUXMA-90021; Cyagen Biosciences) containing FBS, penicillin–streptomycin, dexamethasone, ascorbic acid, glutamine, and β-glycerophosphate. The PCL scaffold, PCL-GelMA scaffold, and blank groups were prepared for comparison. The prepared scaffold extracts were incubated in the culture medium to assess mineralization, and ARS staining was performed on day 14 of osteoinduction. The cells were stained with a 2% ARS solution (Sigma–Aldrich) for 10 min, washed with distilled water, and then quantitatively evaluated for matrix calcification by measuring absorbance at 562 nm after destaining in 10% cetylpyridinium chloride in 10 mM sodium phosphate for 30 min.

2.4.6. Angiogenesis tests

The tube formation assay was conducted to evaluate angiogenesis *in vitro* using a Matrigel basement membrane matrix (356,234; BD Biosciences, CA, USA) following the manufacturer's protocols, and the Transwell assay was conducted to evaluate cell proliferation. Briefly, Matrigel (50 μL/well) was added to 96-well plates using cold pipette tips on ice after overnight thawing at 4 °C. Then, the plates were incubated at 37 °C until the Matrigel became solidified. Next, HUVECs (5×10^4 cells/well) were co-cultured with the extracts from the PCL scaffold, PCL-GelMA scaffold, or the blank groups. Tube formation was evaluated using an inverted microscope after incubation at 37 °C for 6 h. The total length of the tubes was measured using ImageJ software (Media Cybernetics, MD, USA).

HUVECs (1×10^5 cells/well) were co-cultured with the extracts of PCL scaffold or PCL-GelMA scaffold and seeded in the upper chambers of 24-well Transwell plates with 8-μm pore filters (Corning, NY, USA) to perform the Transwell assay. After incubation at 37 °C for 24 h, the cells on the lower surface were stained with 0.1% crystal violet for several minutes after removing the attached cells on the upper surface of the filter membranes. The extent of cell migration was observed using the optical microscope (Leica, Solms, Germany).

2.4.7. Quantitative real-time polymerase chain reaction

The gene expression analysis was performed via real-time quantitative polymerase chain reaction (RT-qPCR) on BMSCs co-cultured with PCL scaffold or PCL-GelMA scaffold after 7 and 14 days ($n = 3$), on HUVECs after 4 and 7 days ($n = 3$), and on chondrocytes co-cultured with GelMA hydrogel of different concentrations after 7, 14, and 21 days. The total cellular RNA was extracted using TRIzol reagent (Invitrogen, CA, USA) and reverse-transcribed into cDNA with a RevertAid First Strand cDNA Synthesis Kit (Thermo Fisher Scientific, MA, USA). qRT-PCR was conducted using the Applied Biosystems StepOnePlus Real-Time PCR System (CA, USA) to evaluate the expression of cartilage-related markers (*COL-II* and *Aggrecan*), osteogenic-related markers (*Runx2* and *OCN*), and angiogenic-related markers (*VEGF* and *ANG-I*), with the housekeeping gene GAPDH used for normalization. The final results were determined using the $2^{-\Delta\Delta Ct}$ method for relative gene expression. The primers used in this study were commercially synthesized (Sangon Biotech, Shanghai, China), and the sequences are listed in Table S2.

2.5. In vivo regeneration of osteochondral defects for the designed scaffolds

2.5.1. Rat osteochondral defect model and treatment

Forty-eight 16-week-old male rats with a body weight of 352 ± 28 g were chosen to create osteochondral defect models to evaluate the repair efficiency of the designed scaffolds. The rats were randomly categorized into 4 groups with 12 rats per group (blank, PCL scaffold, PCL-GelMA scaffold, and biomimetic scaffold). Each animal was shaved and disinfected after general anesthesia, and the surgeries were executed in the exposed right knee joint through a medial parapatellar approach. With the knee in maximal flexion, a full-thickness cartilage defect (2.0 mm in diameter and 1.5 mm in depth) was created in the center of the trochlear groove through the osteochondral cylindrical layer in the femur using an electric drill, as previously described [13]. Afterward, the scaffolds were implanted into the defects. The rats with osteochondral defects without any treatment were used as the blank group. Then, the joint surface was cleaned with sterile saline, and both the capsule and skin were closed. For the first 3 days after surgery, the rats were injected with penicillin to prevent infection. Six rats from each group were euthanized at 12 and 24 weeks post-surgery, and the right knee joints were collected for gross observation, micro-CT evaluation, histological analyses, and immuno-fluorescence analysis. All the rats used in this study were handled following the approved guidelines of the ethics committee of the Shanghai Sixth People's Hospital Affiliated to Shanghai Jiao Tong University School of Medicine (Permit No. DWLL2023-0402).

2.5.2. Gross observation and micro-CT evaluation

The samples from each group were photographed and blindly assessed at specific time intervals by two independent observers in terms of cartilage repair using the International Cartilage Repair Society (ICRS) scoring system. This system evaluated cartilage repair based on criteria such as the extent of defect repair, integration into the border zone, and overall macroscopic appearance. Then, the specimens were fixed in 4% paraformaldehyde for micro-CT evaluation. This assessment involved obtaining 2D and 3D reconstruction images, as well as determining the ratio of bone volume to tissue volume (BV/TV) and trabecular thickness (Tb.Th) of each collected sample.

2.5.3. Histological and immunohistochemical analyses

The joint samples were used for histological and immunostaining analyses, followed by micro-CT scanning, and then demineralized for 8 weeks in 10% EDTA. For the histological analysis, the samples were fixed with 4% paraformaldehyde solution, dehydrated with a series of graded ethanol, and embedded in paraffin. The embedded tissues from each group were sectioned (5 μm thick; Leica, Nussloch, Germany) and stained with hematoxylin and eosin (H&E) and Safranin-O/Fast Green staining. They were then photographed under an optical microscope and evaluated using the ICRS Visual Histological Assessment Scale (ICRS-VHAS) and the O'Driscoll score [32,33].

For immunohistochemical analysis, the sections were rehydrated, blocked, and incubated with primary anti-COL-I, anti-COL-II, anti-Runx2, anti-OCN, and anti-VEGF antibodies (1:100; Abcam) at 4 °C overnight. After incubation with the secondary antibody (1:250; Abcam) at room temperature, the stained sections were visualized using the diaminobenzidine (DAB) substrate and finally counter-stained using hematoxylin.

2.6. Bioinformatics analysis and molecular mechanism

2.6.1. Proteomic and transcriptomic profiling

Simultaneous transcriptome and proteome analyses were performed to explore the key regulators responsible for TA inhibiting angiogenesis. The mRNA expression profiles of TA-treated HUVECs and untreated HUVECs were determined by RNA sequencing. Briefly, total RNA was extracted from cells and ligated with 3' and 5' end adapters. PCR was performed to synthesize first-strand cDNA and for amplification. The cDNA libraries were sequenced using Illumina-Seq for paired-end sequencing. The protocol described by Trapnell et al. was followed for RNA-seq analysis of the generated data [34]. Gene Ontology (GO) term enrichment and Kyoto Encyclopedia of Genes and Genomes (KEGG) pathway enrichment analyses were performed for candidate target genes whose functions were linked with angiogenesis.

Label-free quantification and protein identification were performed to discover the differences in proteomics between the TA-treated and untreated HUVEC groups. Briefly, the total proteins in both groups were purified and digested using a filter-aided sample preparation protocol described by Distler et al. [35]. The extracted ion chromatograms and liquid chromatography with tandem mass spectrometry analysis were used to compare the peak areas to calculate the relative expression levels of each identified protein. The raw files were obtained for analysis by MaxQuant software (Max Planck Institute of Biochemistry, Planegg, Germany). GO and KEGG pathway analyses were performed for bioinformatics analysis.

2.6.2. Western blotting

The total protein concentrations in cells were determined using a BCA protein assay kit (Thermo Fisher Scientific). The cells were lysed in RIPA lysis buffer (Millipore Corporation, MA, USA), and equal amounts of protein were separated by SDS-PAGE gels and transferred to PVDF membranes (Merck Millipore, MA, USA). The blots were blocked with 5% skimmed milk in Tris-buffered saline containing 0.1% Tween-20 for 1 h at room temperature. The membranes were incubated with primary antibodies at 4 °C overnight, followed by incubation with HRP-linked secondary antibodies at 37 °C for 1 h. Western blotting was performed to evaluate the specific protein of interest based on proteomic results and its related proteins in the pathway, including CAV-1 (1:1000; Abcam), β-catenin (1:1000; Abcam), *p*-GSK-3β (1:1000; Abcam), GSK-3β (1:1000; Abcam), and VEGF (1:1000; Abcam). The immunoreactive bands were visualized using enhanced chemiluminescence reagent (Thermo Fisher Scientific) and quantified using ImageJ software.

2.6.3. Cell transfection

HUVECs seeded in 35-mm culture dishes were transfected with a final concentration of 50 nM for siRNAs using Lipofectamine 3000 (Thermo Fisher Scientific). Subsequent experiments were performed after 48 h of incubation. CAV-1 siRNA obtained from RiboBio (Guangzhou, China) was used to knock down the expression of CAV-1 in HUVECs to assess whether CAV-1 knockdown could achieve similar effects on angiogenic function as TA. Briefly, the cells were transfected with si-CAV-1 or si-NC using Lipofectamine 3000 following the manufacturer's protocols.

2.7. Statistical analysis

All quantitative data were presented as the mean $\pm$ standard deviation, and statistical analyses were performed using GraphPad Prism 9.0. The groups were compared using one-way analysis of variance followed by Tukey's *post hoc* test for multiple comparisons. A *P* value < 0.05 indicated a statistically significant difference.

3. Results

3.1. Fabrication and characterization of 3D-printed biomimetic scaffold

A multi-materials 3D printing approach was employed to fabricate the proposed biomimetic scaffold (Fig. 2a). Initially, the FDM 3D printing technique was used to fabricate the PCL scaffold, which served as a bottom layer. A uniform and interconnected porous structure with a pore size of 200 μm was printed to facilitate the subchondral bone regeneration (Fig. 2b). The Young's modulus of the porous PCL scaffold was measured to be 89.3 ± 8.74 MPa (Fig. 2c). This modulus was in the
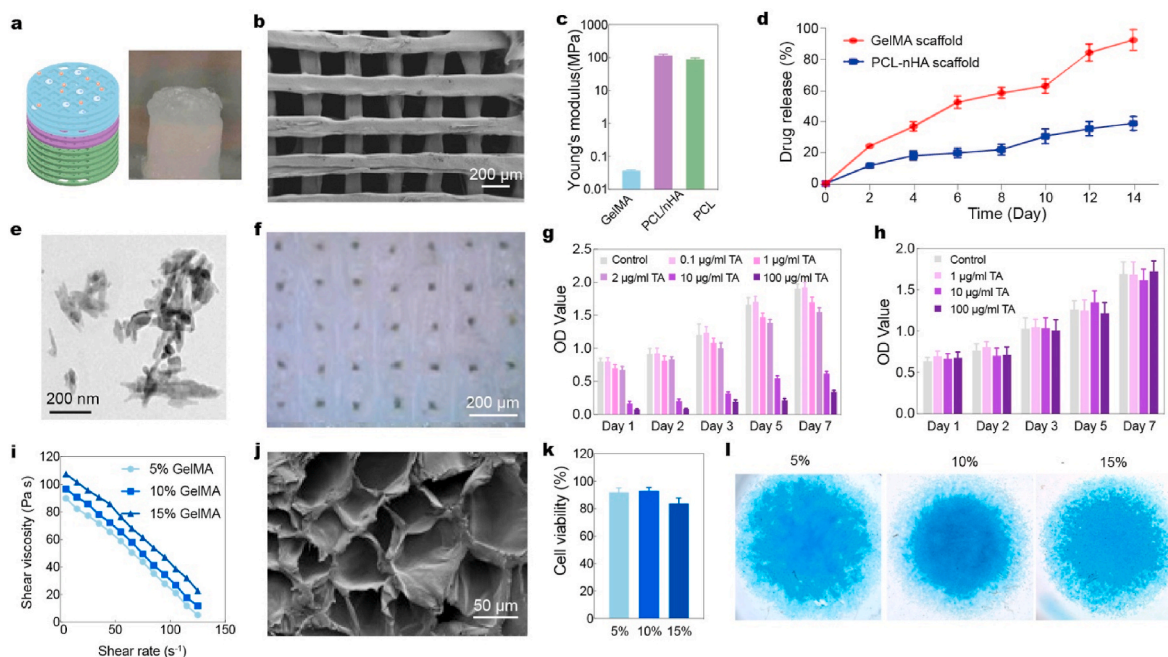
Fig. 2. Preparation and characterization of the biomimetic scaffold. (a) Schematic illustration (left) and photograph (right) for the biomimetic scaffold; (b) Scanning electron microscopy (SEM) image of porous bottom layer in the biomimetic scaffold; (c) Young's modulus of the top GelMA layer, the interfacial PCL-nHA layer, and the bottom PCL layer; (d) Drug release profile in the GelMA and PCL-nHA scaffolds; (e) Transmission electron microscopy (TEM) image of the nHA; (f) Macroscopic image of compact calcified interfacial layer; (g) CCK-8 assay for the proliferation of HUVECs cultured with different concentration of tasquinimod for 7 days; (h) CCK-8 assay for the proliferation of chondrocytes cultured with the concentrations of tasquinimod for 7 days; (i) Shear viscosity as a function of shear rate for the 5%, 10%, and 15% GelMA, respectively; (j) SEM image of the porous top GelMA layer; (k) Qualification of live/dead staining of chondrocytes co-cultured with different concentrations of GelMA; (l) Alcian blue staining of chondrocytes co-cultured with different concentrations of GelMA.

range of native spongy bone stiffness (55–480 MPa) [36], making it suitable for promoting osteogenic differentiation of BMSCs [37]. BMSCs were cultured with porous PCL scaffolds for 7 days to assess the cytocompatibility of PCL scaffolds and evaluate cell differentiation. The results indicated low cytotoxicity and high biocompatibility, as evidenced by a significant increase in live cells (green) on PCL scaffold surfaces (Fig. S1).

To create a biological barrier, TA was introduced in the scaffold and gradually released from the GelMA and calcified interfacial layer. The TA release profile was quantified, showing that 40% and 100% of the total loaded drug was released from the calcified interfacial layer and GelMA layer at two weeks, respectively. nHA particles were embedded into the PCL scaffold to establish a calcified interfacial layer serving as a physical barrier between the top and bottom layers. The nHA particles, with 200–500 nm length and 20–30 nm diameter, were distributed within the PCL scaffold (Fig. 2e), resulting in a compact structure (Fig. 2f). In addition, the compressive modulus of PCL-nHA was slightly higher than that of PCL ($P < 0.05$), and PCL-nHA also exhibited significant tensile strength ($P < 0.01$) (Fig. 2c). The concentration of TA was further optimized through co-culturing with HUVECs (Fig. 2g) and rat primary chondrocytes (Fig. 2h). CCK-8 assays revealed that the HUVECs treated with 10 μg/mL TA exhibited significantly decreased cell viability (Fig. 2g). However, no significant differences were observed among all TA groups and the control group (0 μg/mL) for rat primary chondrocytes, indicating that TA had no cytotoxic effect on chondrocytes (Fig. 2h). Based on these results, 10 μg/mL TA was selected for further experiments.

Primary rat chondrocytes were first isolated from femoral heads and condyles of SD rats to prepare the bioink for cartilage repair. Lyophilized GelMA was then dissolved in DMEM media and combined with TA and primary rat chondrocytes. The successful chemical functionalization of GelMA was confirmed by nuclear magnetic resonance (^{1}H NMR) and FTIR analysis (Fig. S2). The concentrations of GelMA in the bioinks were first optimized within 5%–15% range. As the GelMA concentration

increased, the bioinks showed enhanced printability with higher shear-thinning and shear-yielding properties (Fig. 2i). The printed top scaffold showed porous networks with a diameter of approximately 200 μm, enabling cell migration and proliferation (Fig. 2j) [38]. Furthermore, the printed top scaffolds exhibited a lower water absorption, and lower degradation rate as the GelMA concentration increased (Fig. S3). Live/dead staining was conducted to evaluate the adhesion and viability of the rat primary chondrocytes seeded on the GelMA with different concentrations (Fig. S4). Cell viability results indicated that 5% and 10% GelMA supported chondrocyte growth and demonstrated favorable biocompatibility without significant cytotoxicity. However, 15% GelMA exhibited reduced viability, suggesting that a higher GelMA concentration decreased cell metabolic activities (Fig. 2k) [39].

Cell-loaded hydrogels were evaluated by alcian blue staining and RT-qPCR to further assess the biological effect of GelMA on the chondrogenic activity of chondrocytes. Alcian blue staining revealed that 10% GelMA exhibited the highest efficacy in promoting chondrogenesis (Fig. 2l). The gene expression levels of COL-II and Aggrecan were significantly higher in the 5% GelMA and 10% GelMA groups compared with the 15% GelMA group ($P < 0.05$) on day 7. The 5% GelMA group showed the highest gene expression, which slightly surpassed that in the 10% GelMA group on days 14 and 21 (Fig. S5). Considering printability and physicochemical properties, 10% GelMA was chosen for further experiments.

3.2. In vitro biocompatibility tests

Cell migration and growth are essential aspects of tissue repair and regeneration. The osteogenic and angiogenic regenerative capabilities of the top GelMA and bottom PCL scaffolds were first characterized through *in vitro* culturing BMSCs and HUVECs, respectively. The control group involved cell culture without the scaffolds. The proliferation of BMSCs showed no significant difference between the PCL-GelMA and PCL scaffolds (Fig. 3a). However, the proliferation of HUVECs was
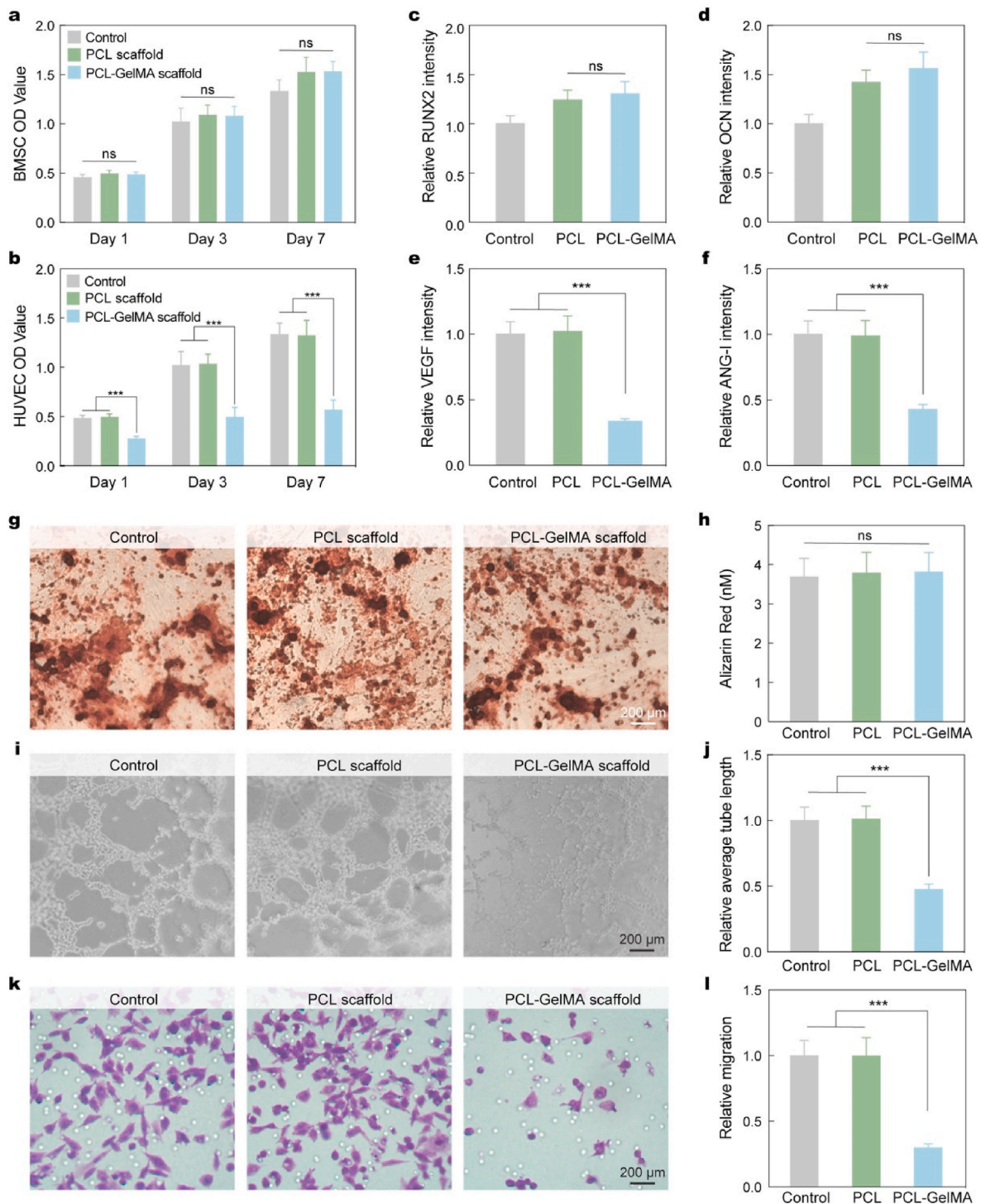
Fig. 3. In vitro biocompatibility evaluation of scaffolds. a, b) The proliferation of BMSCs (a) and HUVECs (b) for control group, PCL scaffold, and PCL-GelMA scaffold; c-f) The osteogenic mRNA expression levels of *Runx2* (c) and *OCN* (d), and the angiogenic mRNA expression levels of *VEGF* (e) and *ANG-I* (f) for control group, PCL scaffold, and PCL-GelMA scaffold, respectively; g, h) Microscropic images (g) and quantitative analysis of Alizarin Red S (h) of osteogenic differentiation after 14 days incubation of BMSCs for control group, PCL scaffold, and PCL-GelMA scaffold, respectively; i, j) Microscopic images of tube formation by HUVECs (i) and quantitative analysis (j) of the average tube length; k, l) Transwell assay (k) and quantitative analysis (l) of the cell migration rate for control group, PCL scaffold, and PCL-GelMA scaffold. (***) p < 0.001; ns = no significance.

significantly inhibited in the PCL-GelMA scaffold (*P* < 0.001, Fig. 3b). These results indicated that both PCL-GelMA and PCL scaffolds had high osteogenic regenerative capabilities, whereas the PCL-GelMA scaffold exhibited a reduced angiogenic regenerative capability. The gene expression of key osteogenic makers, such as Runt-related transcription factor-2 (*Runx2*, Fig. 3c) and osteocalcin (*OCN*, Fig. 3d), gradually

increased over time. Both the PCL-GelMA and PCL scaffolds slightly enhanced the expression of osteogenic genes compared with that in the control group, indicating a high biocompatibility. Additionally, the expression of angiogenic genes, such as *VEGF* and *ANG-I*, was substantially downregulated in the PCL-GelMA scaffold compared with the PCL scaffold (Fig. 3e and **f**). Collectively, these findings revealed that both

the PCL-GelMA and PCL scaffolds exhibited osteogenic activity, whereas the PCL-GelMA scaffold inhibited angiogenesis *in vitro*. For osteogenic differentiation, the results of ARS showed no difference among all groups (Fig. 3g), and the quantitative results further confirmed no significantly more calcium accumulation (Fig. 3h). Transwell and tube formation assays were performed to determine the effects of these scaffolds on pro-angiogenic activity. HUVECs co-cultured with PCL-GelMA scaffold migrated much slower than those co-cultured with PCL scaffold and control group after incubation for 24 h ($P < 0.001$) (Fig. 3i–l). Furthermore, HUVECs co-cultured with PCL scaffold could generate more cord-like structures on Matrigel than those co-cultured with PCL-GelMA scaffold.

3.3. Biomimetic scaffold facilitated the regeneration of osteochondral defects in vivo

3.3.1. Macroscopic and micro-CT observation

Three types of scaffolds, including monolayer scaffold (porous PCL), bilayer scaffold (PCL-GelMA scaffold without calcified interfacial layer), and biomimetic scaffold (without calcified interfacial layer), were implanted into rat osteochondral defects for 12 and 24 weeks to evaluate the role of the calcium interfacial layer in the biomimetic scaffold for integrative osteochondral repair. Macroscopic, 2D and 3D micro-CT observations were conducted to evaluate the efficiency in the three groups, along with a blank control group (Fig. 4a–d). In the blank group, the defects remained unfilled, and a small amount of fibrous tissue with a rough surface was visible at 12 weeks post-implantation (Fig. S6). Even

after 24 weeks, the defects remained concave and showed no signs of repair (Fig. 4a). For PCL and PCL-GelMA scaffolds, the defect sites exhibited a rough surface, and the margins around the defect sites were still obvious (Fig. 4b and c). However, the newly formed tissues were smooth and the margins became indistinct in the biomimetic scaffold group. Notably, the surface cartilage showed slight repair in the PCL-GelMA scaffold group, with a rough surface and distinctive morphology compared with the native cartilage (Fig. 4c). In contrast, the defects in the biomimetic scaffold group were filled with cartilage-like tissues and repaired completely. The newly formed cartilaginous tissues integrated with the surrounding native cartilage without obvious margins (Fig. 4d). Also, a macroscopic grading scale based on ICRS scoring system was used to quantitatively evaluate regeneration efficiency. The total score in the biomimetic scaffold group was significantly higher than that in the other groups in 12 and 24 weeks (Fig. S7). Similarly, an increased calculation of bone volume fraction (BV/TV) in the biomimetic scaffold group confirmed a higher amount of calcified tissue, indicating a more efficient regeneration for the scaffold with a calcified interfacial layer (Fig. S7).

3.3.2. Histological examination

The H&E and Safranin-O/Fast Green staining histological analyses were further performed to assess osteochondral repair. In the blank group, partial repair with collagen filling was observed in 12 weeks, whereas the subchondral bone collapsed and disordered, loose, and fibrous tissues covered the surface of defects at 24 weeks. Notably, fibrous tissues rather than bone-like tissues filled the deeper regions of
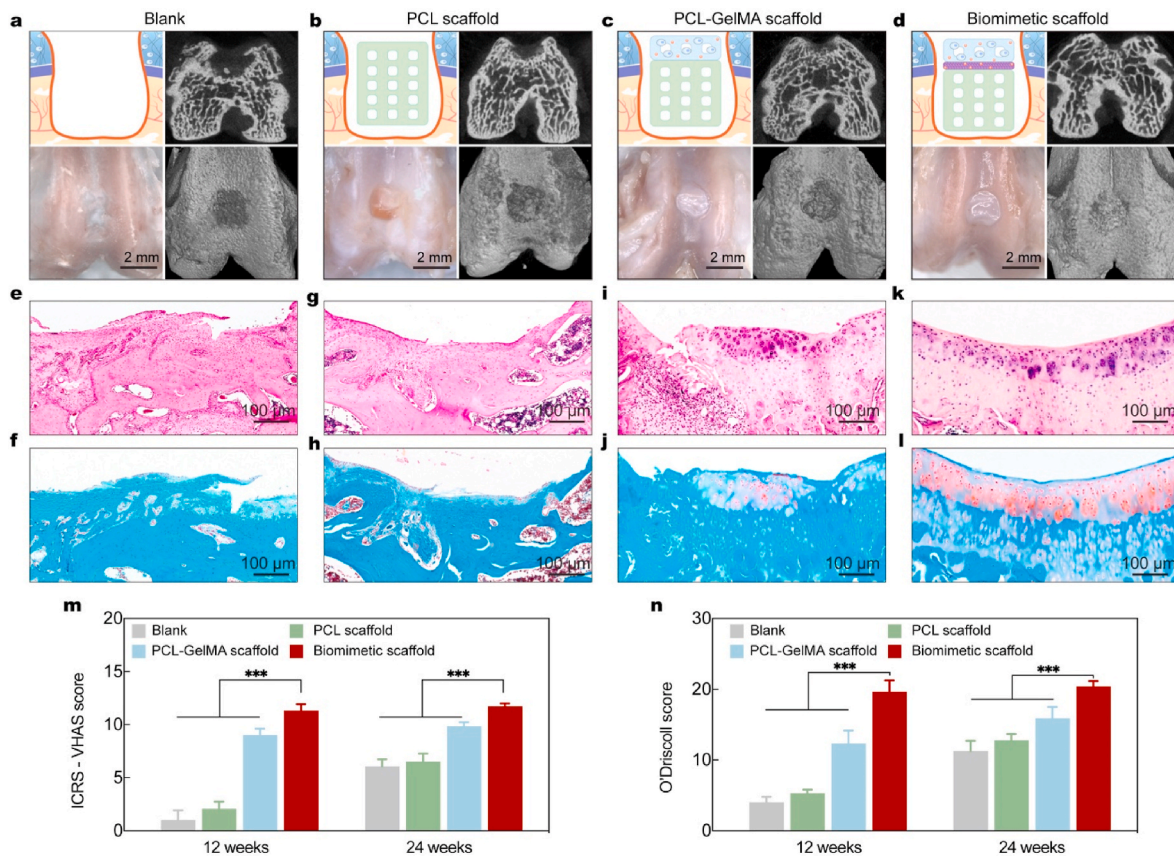
Fig. 4. In vivo evaluation of the biomimetic scaffold. a-d) Schematic illustration (top left), gross views (bottom left), 2D (top right) and 3D (bottom right) micro-CT images of bone formation at 24 weeks post-operation for blank (a), PCL scaffold (b), PCL-GelMA scaffold (c), and biomimetic scaffold (d), respectively; e-l) H&E staining and Masson's trichrome staining of osteochondral defects without scaffold implantation (e, f) and with the implantation of PCL scaffold (g, h), PCL-GelMA scaffold (i, j), and biomimetic scaffold (k, l) for 24 weeks, respectively; m, n) International Cartilage Repair Society Visual Histological Assessment Scale (ICRS-VHAS) (m) and O'Driscoll (n) score to evaluate the osteochondral regeneration for blank group, PCL scaffold, PCL-GelMA scaffold, and biomimetic scaffold at 12 and 24 weeks post-implantation, respectively. (***) p < 0.001.

the defects (Fig. 4e and f). For the PCL scaffold, some cancellous bone formation occurred in the subchondral layer of the defects with a small amount of fibrous-cartilage-like tissues on the surface (Fig. 4g and h). In the PCL-GelMA scaffold group, incomplete repair was observed in 12 weeks, with a larger amount of cartilage-like tissue than in the blank and PCL scaffold groups (Fig. S8). In 24 weeks, newly formed bone tissues were observed in the deeper regions, whereas a limited number of cartilaginous tissues were formed on the surface (Fig. 4i and j). In the biomimetic scaffold group, a gap existed between the repaired tissue and normal cartilage in 12 weeks post-operation, but the repaired tissues were almost completely fused with the normal cartilage in 24 weeks (Fig. 4k and l). The effectiveness of regeneration was further evaluated using the ICRS-VHAS and O'Driscoll scores. The biomimetic scaffold group consistently achieved significantly higher scores compared with those in the other groups in both 12 and 24 weeks (Fig. 4m and n).
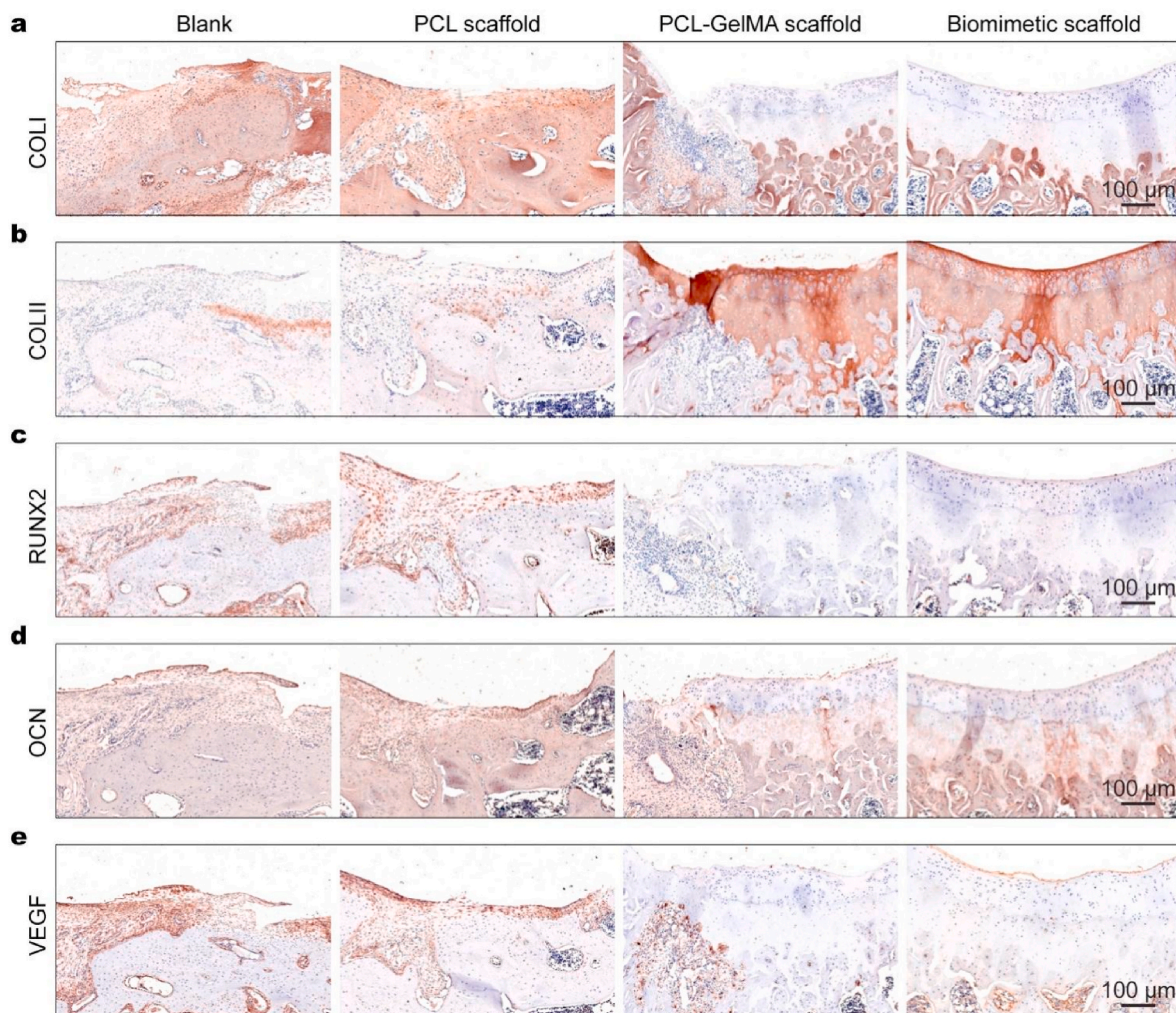
3.3.3. Immunohistochemical assay

Immunohistochemical staining was further performed to analyze chondrogenesis and osteogenesis in each group. Positive expression of collagen II, indicative of cartilage formation, was observed exclusively in the newly formed cartilage in the biomimetic scaffold group in 12 weeks post-implantation (Fig. S9). In both PCL-GelMA and biomimetic scaffold groups, the lower expression of collagen I and higher expression of collagen II were observed on the surface region of the defect sites in

24 weeks post-implantation, suggesting ongoing cartilage development (Fig. 5a and b). Regarding osteogenesis markers, the expression of RUNX2 and OCN was observed in the defect sites of all the groups in 12 weeks (Fig. S9). However, in 24 weeks, positive expression of RUNX2 was limited on the surface area of the defect sites in the blank and PCL scaffold groups (Fig. 5c). Regarding OCN, positive responses were found in the whole defect area in the PCL scaffold and blank groups. In contrast, positive expression was observed in only the subchondral bone area, but negative expression was reported in the cartilaginous tissue in the PCL-GelMA scaffold and biomimetic scaffold groups (Fig. 5d). The results of immunohistochemical staining were consistent with the findings of Safranin-O/Fast Green staining (Fig. 4e–4l), suggesting that the biomimetic scaffold enabled further promotion of hyaline cartilage regeneration. The expression of VEGF was assessed to evaluate vessel invasion into the cartilage layer. Interestingly, only the cartilage layer in the biomimetic scaffold group showed negative VEGF expression at both time points (Fig. 5e), suggesting that the calcified interfacial layer successfully prevented vessel invasion into the cartilage layer *in vivo*.

3.4. Downregulating CAV-1 inhibited angiogenesis via Wnt/β-catenin pathway

TA was found to have an anti-angiogenic effect [20] and inhibited endothelial cell proliferation, migration, and lumen formation [21]. We

Fig. 5. Immunohistochemical analysis of osteochondral regeneration. (a, b) Immunohistochemical staining of the chondrogenic marker COL I (a) and COL II (b) at 24 weeks post-operation, respectively; (c, d) Immunohistochemical staining of the osteogenic marker RUNX2 (c) and OCN (d) at 24 weeks post-operation, respectively; (e) Immunohistochemical staining of the angiogenic marker VEGF at 24 weeks post-operation.
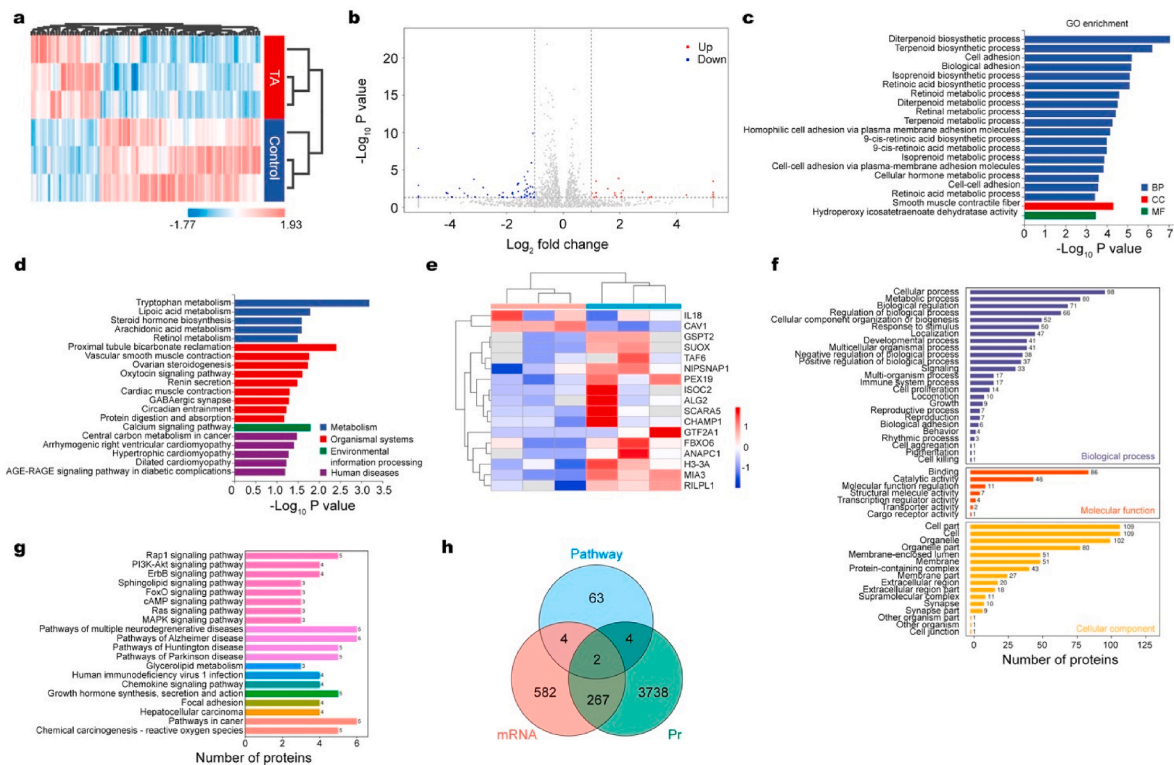
Fig. 6. RNA-sequencing transcriptomics and label-free proteomics for identification differential genes and proteins. (a) Heat map of genes with differential expression between TA and control groups. Blue and red colors indicate downregulation and upregulation, respectively; (b) Volcano plot of RNA sequencing analysis of mRNAs with differential expression between TA and control groups. Blue and red colors indicate downregulation and upregulation, respectively; (c, d) GO analysis (c) and KEGG analysis (d) of different expressed genes; (e) The heat map of top 17 key proteins for differential expression; f) GO enrichment analysis of different expressed proteins according to biologic process, cellular component, and molecular function; (g) KEGG analysis of different expressed proteins; (h) Venn diagram showing that two genes (CAV-1 and IL-18) are obtained after cross-analysis of genes in RNA-seq, protein profiles and angiogenesis pathway. TA, tasquinimod; GO, Gene ontology; KEGG, Kyoto Encyclopedia of Genes and Genomes.

conducted RNA-sequencing transcriptomic and label-free proteomic analyses on TA-treated HUVECs compared with the non-treated group to investigate the introduction of TA for inhibiting neovascularization and the mechanism of angiogenesis inhibition. This allowed us to identify differentially expressed genes and proteins. The heatmap and volcano plot showed that 35 mRNAs were upregulated while 72 mRNAs were downregulated in the TA-treated group compared with the control group, with log$_2$-fold change >2 or <0.5 and $P < 0.05$ (Fig. 6a and b). GO and KEGG pathway enrichment analyses of differentially expressed genes are illustrated in Fig. 6c 6d. Simultaneously, 4011 differentially expressed proteins were identified as quantifiable between the two groups, and the heatmap illustrated the top 17 key proteins comparatively with respect to the log$_2$-fold change and P value (Fig. 6e). GO and KEGG pathway enrichment analyses of differentially expressed proteins are depicted in Fig. 6f and **g**. The Venn diagram results showed that two genes (CAV-1 and IL-18) were obtained after the cross-analysis of genes in RNA-seq, protein profiles, and angiogenesis pathway (Fig. 6h). CAV-1 interacted with some well-known angiogenic (pro-angiogenic) factors, such as VEGF, basic fibroblast growth factor, or hepatocyte growth factor. On the one hand, CAV-1 activated VEGFR-2 via a VEGF-dependent pathway, and the removal of caveolin and VEGFR-2 from caveolae led to the inhibition of endothelial cell migration; on the other hand, CAV-1 was also essential for NO (nitric oxide)-mediated angiogenesis, and VEGF promoted the production of NO and the formation of capillary-like tubules [40]. Interestingly, some studies reported that the knockdown of CAV-1 expression enhanced osteogenic differentiation through the calcium signaling pathway; however, no studies indicated the connection between IL-18 and osteochondral defects [41].
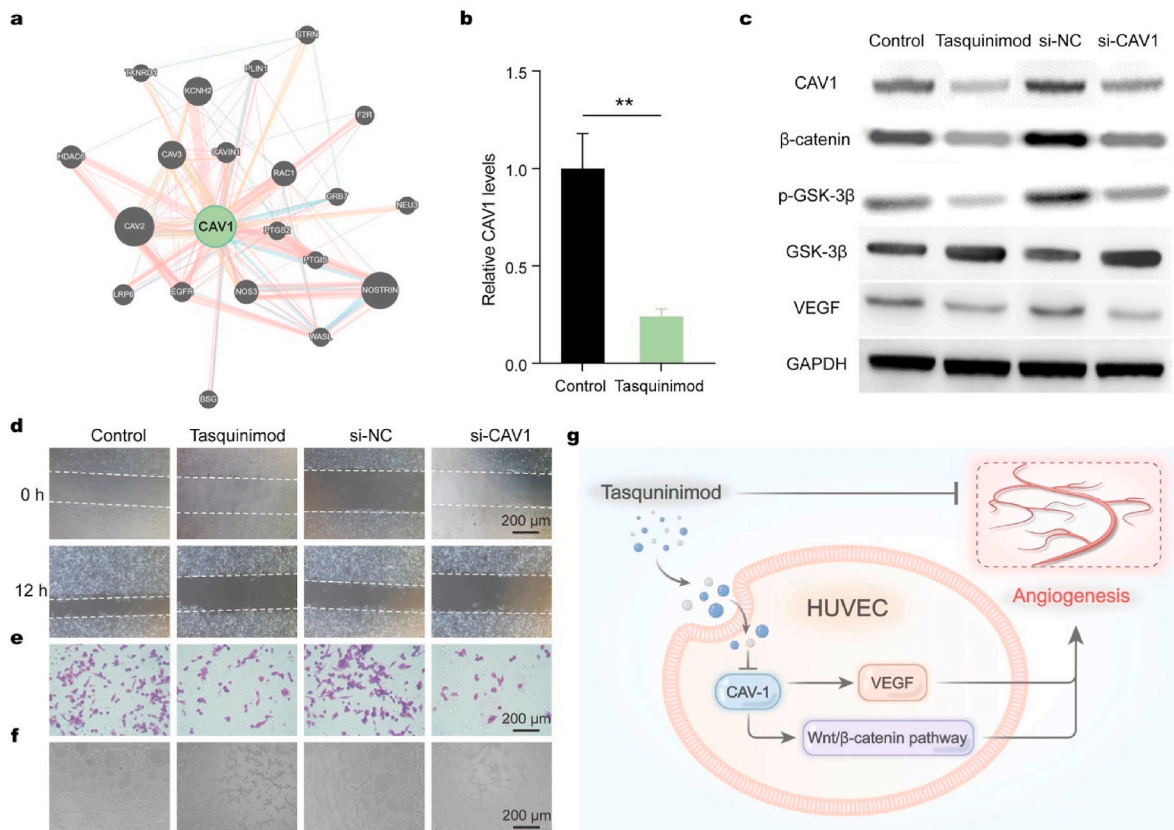
The protein–protein interaction analysis revealed the interaction

between CAV-1 and angiogenic genes (Fig. 7a). RT-qPCR indicated that the level of CAV-1 significantly reduced when HUVECs were treated with TA (Fig. 7b). We transfected si-CAV-1 and negative control siRNA (si-NC) into HUVECs to verify that silencing CAV-1 had the same effect as TA on proliferation, migration, and angiogenesis. CAV-1 was a positive regulator of endothelial cell proliferation, angiogenesis, and migration, along with our loss-of-function assay results (Fig. 7c–e). We confirmed that the TA drug and si-CAV-1 could inhibit proliferation, angiogenesis, and migration in HUVECs by scratch wound, Transwell, and tube formation assays. Studies showed that CAV-1 could target VEGF in HUVECs to induce the activation of the Wnt/β-catenin pathway, and the activation of the Wnt/β-catenin signaling pathway could stimulate multiple critical steps in angiogenesis [42]. Western blotting images revealed that both the TA drug and si-CAV-1 induced significant decreases in β-catenin expression and phosphorylation of GSK-3β (Fig. 7f). These findings indicated that TA blocked angiogenesis by inhibiting CAV-1 in HUVECs, and CAV-1 promoted angiogenesis via the Wnt/β-catenin pathway (Fig. 7g). The findings from both proteomics and transcriptomics in this study indicated that CAV-1 played a crucial role in angiogenesis during the repair of osteochondral defects and could be significantly reduced by TA drugs. Knocking down CAV-1 in HUVECs might inhibit vascularization via the Wnt/β-catenin pathway, subsequently downregulating VEGF.

4. Discussion

In recent years, the trilayer scaffold has been considered more suitable for repairing osteochondral defects, as the bilayer scaffold was reported to have issues such as excessive cartilage downgrowth into the subchondral bone and insufficient cartilage regeneration in

Fig. 7. Gene and protein expression analysis revealing CAV-1 promoted angiogenesis by Wnt/β-catenin pathway. (a) The protein-protein interactions analysis revealing the interaction between CAV-1 and angiogenic genes. (b) RT-qPCR confirmation of the low level of CAV-1 in TA-treated group; (c) Western blotting assay for the protein expression of CAV-1, β-catenin, GSK-3β, *p*-GSK-3β, and VEGF after transfection with si-CAV-1 or negative control (NC); (d) Representative images showing the migration ability of HUVECs at 12 h by scratch wound assay; (e, f) Migrated HUVECs using the transwell assay (e), and tube formation in HUVECs (f) after transfection with si-CAV-1 or NC. The white dashed lines are the edges of the cell migration; (g) Schematic illustration of the mechanism showing that TA blocked angiogenesis through inhibiting of CAV-1 in HUVECs, and CAV-1 promoted angiogenesis by activating Wnt/β-catenin pathway. (**) p < 0.01.

osteochondral defect repair [43]. For example, Liu et al. fabricated the nanofibrous membrane unit functioning as the middle layer for mimicking the calcified layer, which was found to be permeable to some molecules with limited molecular weight and could prevent the seeded cells from migrating across the unit [44]. A similar phenomenon was observed *in vivo* when the interface layer was absent in our study. However, the invasion of regenerated cartilage tissue toward the subchondral bone and the vascularization of hyaline cartilage were blocked by the natural calcified interfacial layer. Some studies showed that the calcified interfacial zone was dense with a "tooth comb" shape, coinciding with the subchondral bone. The main components were collagen II (20.16 ± 0.96)% and hydroxyphosphate (65.09 ± 2.31)%. The thickness of the calcified interfacial layer was 104.16 ± 20.87 μm, compressive modulus was (208.6 ± 39.7) MPa, and tensile modulus was (178.3 ± 35.9) MPa, 10 times harder than hyaline cartilage, but 1/60 than subchondral bone [45,46]. Given these special morphological characteristics and composition, the mechanical impact attenuated significantly during knee joint motion. More importantly, the shear force of articular cartilage could be converted into compressive stress by the calcified interfacial zone and transferred to the subchondral bone, thus significantly reducing the likelihood of crushing and tearing the articular cartilage [47]. In addition, the calcified interfacial zone might block the exchange of materials between the articular cartilage and the subchondral bone. As a result, the cartilage and the subchondral bone were separated into relatively independent physiological environments by this thin structure [48]. In the present study, we fabricated the calcified interfacial layer printed with FDM using nHA and PCL, which enhanced mechanical properties and layer-specific barrier function.

Combining TA could completely block angiogenesis in the hyaline cartilage. Similarly, Jia et al. developed a multilayered scaffold with the bone layer 3D-printed with PLGA/TCP. The cartilage layer was a temperature gradient–oriented hydrogel, the compact layer was a seamless layer produced using 3D printing, and the intermediate compact interfacial layer hardly afforded an avascular microenvironment in the upper cartilage layer [49].

Compared with mono- or bilayer scaffolds, constructing trilayer scaffolds is complicated, as it is challenging to forge three different structures into one construct in a single step. Most trilayer scaffolds were made up of different parts fabricated separately, leading to problems such as changes in mechanical properties and dissociation of multiple layers after implantation [50]. Zhai et al. used the "twice freeze-drying" technique to construct a dense isolation layer with a high concentration of chitosan/gelatin solution [51]. Qiao et al. designed and fabricated a trilayered stratified scaffold in which a cell-laden GelMA with zone-specific growth factor delivery was combined with fiber organization and networks [29]. However, these attempts could hardly mimic the connecting manner and mechanical features in native tissue, and each printed construct was assembled discontinuously or in several steps. In our study, we fabricated the trilayer scaffold in one step by switching the nozzles of FDM and extrusion bioprinting. With the development of multi-nozzle printing technology, the range of materials for constructing complex 3D models significantly expanded; however, coordinating different nozzles and materials still involved many details [52,53]. A few differences based on the type of bioinks and cells were observed in terms of printing cell-laden hydrogels. In this study, various parameters, including the GelMA concentration ratio, the inner table of

the nozzles, the printing temperature, and the printing speed, were repeatedly adjusted to ensure high fidelity and high cell viability (greater than 90%). The key point in the printing of PCL and PCL-nHA was adjusting the printing temperature and speed. The challenge in this study was coordinating the two nozzles and materials well to simultaneously guarantee structural stability and desired mechanical properties. Moreover, GelMA and chondrocytes needed to be protected from the high temperature of 70 °C during the PCL and PCL-nHA printing process, and the hydrogel printing temperature of 21 °C was determined based on the gelatin kinetics.

The use of 3D printing for treating osteochondral defects can be categorized into two main approaches: scaffold-based approaches and direct 3D printing approaches [54]. Scaffold-based approaches involve the fabrication of a 3D scaffold, which is then seeded with cells and biocompatible materials and implanted into the defect. On the contrary, direct 3D printing approaches involve the direct printing of cells, biomaterials, or a combination of both into the defect to form a living tissue construct. Scaffold-based approaches face challenges because the scaffolds can easily become damaged during implantation, affecting the distribution of cells and biomaterials and resulting in impaired tissue regeneration [55]. Direct 3D printing approaches have limitations related to the resolution of the printing process, making it difficult to create complex tissue architectures with precise control over cell and biomaterial distribution. In addition, the printing process may cause cell death due to the mechanical stress of the printing process or low oxygen levels in the printed construct [13,56]. In this study, we presented a new hybrid bioprinting approach to build zonally stratified articular cartilage to mimic the anatomy of native cartilage using primary chondrocytes. The cell viability and mechanical properties were the preliminary criteria used to verify the success of the 3D-printed multiphase biological scaffold. The data in this study demonstrated the feasibility of the printing construct and the good cytocompatibility of the materials used.

Consistent with previous studies, CAV-1 si-RNA treatment directly downregulated GSK3 and β-catenin transcriptional activity, thereby inhibiting VEGF, suggesting that CAV-1 promotes angiogenesis by the Wnt/β-catenin pathway. Notably, CAV-1 is part of the canonical Wnt pathway and a crucial component of the caveolae machinery [57]. On the one hand, CAV-1 activates VEGFR-2 via a VEGF-dependent pathway and the removal of caveolin and VEGFR-2 from caveolae leads to the inhibition of endothelial cell migration. On the other hand, CAV-1 is also essential for nitric oxide (NO)-mediated angiogenesis, whereas VEGF promotes the production of NO and the formation of capillary-like tubules. Ding et al. transfected antisense CAV-1 oligonucleotides into HUVECs, resulting in a significant decrease in the number of capillary-like tubules, and NO production did not respond to the addition of VEGF and a nonselective NOS (NO synthase) inhibitor [58]. The results of proteomics and transcriptomics in this study indicated that CAV-1 was a critical regulator of angiogenesis in repairing osteochondral defects, and its expression was significantly reduced by TA drugs. Knocking down CAV-1 in HUVECs might inhibit vascularization via the Wnt/β-catenin pathway and downregulate VEGF.

Several areas warrant further investigation. First, considering the extreme complexity of the osteochondral unit, the trilayer scaffolds used in this study provided a simplified representation. Developing scaffolds that better mimic the complex structure could potentially enhance the effectiveness of osteochondral repair. Second, the multiple extrusion printing methods employed in this study may potentially induce breaks or defects between different layers. More advanced continuous additive manufacturing technologies can be explored to facilitate the fabrication of artificial implants with improved structural integrity. Third, it would be possible to precisely determine the thickness, morphology, and structure of each scaffold layer by leveraging 3D imaging technology to reconstruct the osteochondral defect, thus ensuring a more accurate correspondence to the cartilage defect. Notably, choosing cell sources has always been considered a bottleneck in cartilage repair [59]. While

this study used primary chondrocytes, autologous BMSCs may offer a promising alternative due to their convenient acquisition and ease of expansion *in vitro*. Exploring the potential mechanism of BMSCs differentiating into hyaline cartilage would be a valuable area for future investigation.

5. Conclusions

In this study, a biomimetic scaffold containing a calcified interfacial layer was designed and fabricated to repair osteochondral defects in rats. The combination of chondrogenic and osteogenic regeneration in distinct microenvironments, as a 3D-printed integrated scaffold, was achieved in one step by switching the nozzles of FDM and extrusion bioprinting. This approach resulted in a noticeable synergistic effect, enhancing both chondrogenesis and osteogenesis. At 24 weeks postoperatively, the repair outcome in the biomimetic scaffold group surpassed those in the PCL scaffold and PCL-GelMA scaffold groups. Our data suggested the essential role of the calcified interfacial layer in this procedure, emphasizing the importance of simulating the natural physiological and mechanical environments during osteochondral defect repair. In addition, TA used in the calcified interfacial layer could block angiogenesis by inhibiting CAV-1 and inactivating the Wnt/β-catenin signaling pathway. Overall, the 3D-printed biomimetic scaffold exhibited useful biological properties and mimicked the spatially varying properties of native osteochondral tissue, both *in vitro* and *in vivo*. It demonstrated high performance in the reconstruction of articular cartilage and subchondral bone, providing a promising candidate for functional osteochondral regeneration.

Ethics approval and consent to participate

All of the rats utilized in this study were treated according to the guidelines approved by the ethics committee of the Shanghai Sixth People's Hospital Affiliated to Shanghai Jiao Tong University School of Medicine (Permit No. DWLL2023-0402).

CRediT authorship contribution statement

Di Wu: Writing – review & editing, Writing – original draft, Methodology, Funding acquisition, Formal analysis, Conceptualization. **Kaiwen Zheng:** Writing – original draft, Methodology, Data curation. **Wenjing Yin:** Writing – review & editing, Data curation. **Bin Hu:** Visualization, Validation, Methodology. **Mingzhao Yu:** Software, Methodology. **Qingxiao Yu:** Software, Formal analysis. **Xiaojuan Wei:** Writing – review & editing, Supervision, Investigation, Conceptualization. **Jue Deng:** Writing – review & editing, Resources, Project administration. **Changqing Zhang:** Supervision, Resources, Funding acquisition.

Declaration of competing interest

There are no conflicts to declare.

Acknowledgments

Appendix A. Supplementary data

Supplementary data to this article can be found online at https://doi.org/10.1016/j.bioactmat.2024.03.004.

References

[1] K. Ching, et al., Hypertension meets osteoarthritis - revisiting the vascular aetiology hypothesis, Nat. Rev. Rheumatol. 17 (9) (2021) 533–549.

[2] S.R. Goldring, M.B. Goldring, Changes in the osteochondral unit during osteoarthritis: structure, function and cartilage-bone crosstalk, Nat. Rev. Rheumatol. 12 (11) (2016) 632–644.

[3] H. Kwon, et al., Surgical and tissue engineering strategies for articular cartilage and meniscus repair, Nat. Rev. Rheumatol. 15 (9) (2019) 550–570.

[4] E.A. Makris, et al., Repair and tissue engineering techniques for articular cartilage, Nat. Rev. Rheumatol. 11 (1) (2015) 21–34.

[5] C. Madeira, et al., Advanced cell therapies for articular cartilage regeneration, Trends Biotechnol. 33 (1) (2015) 35–42.

[6] S.P. Nukavarapu, D.L. Dorcemus, Osteochondral tissue engineering: current strategies and challenges, Biotechnol. Adv. 31 (5) (2013) 706–721.

[7] R. Chen, et al., Multiphasic scaffolds for the repair of osteochondral defects: outcomes of preclinical studies, Bioact. Mater. 27 (2023) 505–545.

[8] C. Lesage, et al., Material-assisted strategies for osteochondral defect repair, Adv. Sci. 9 (16) (2022) e2200050.

[9] S. Camarero-Espinosa, et al., Directed cell growth in multi-zonal scaffolds for cartilage tissue engineering, Biomaterials 74 (2016) 42–52.

[10] S.M. Hull, L.G. Brunel, S.C. Heilshorn, 3D bioprinting of cell-laden hydrogels for improved biological functionality, Adv. Mater. 34 (2) (2022) e2103691.

[11] C.F. Guimaraes, et al., Engineering hydrogel-based biomedical photonics: design, fabrication, and applications, Adv. Mater. 33 (23) (2021) e2006582.

[12] S.H. Kim, et al., 3D bioprinted silk fibroin hydrogels for tissue engineering, Nat. Protoc. 16 (12) (2021) 5484–5532.

[13] F. Gao, et al., Direct 3D printing of high strength biohybrid gradient hydrogel scaffolds for efficient repair of osteochondral defect, Adv. Funct. Mater. 28 (13) (2018).

[14] W. Dang, et al., 3D printing of Mo-containing scaffolds with activated anabolic responses and bi-lineage bioactivities, Theranostics 8 (16) (2018) 4372–4392.

[15] C. Deng, et al., Bioactive scaffolds for regeneration of cartilage and subchondral bone interface, Theranostics 8 (7) (2018) 1940–1955.

[16] F. Pati, et al., Ornamenting 3D printed scaffolds with cell-laid extracellular matrix for bone tissue regeneration, Biomaterials 37 (2015) 230–241.

[17] X. Wang, et al., Identification of an ultrathin osteochondral interface tissue with specific nanostructure at the human knee joint, Nano Lett. 22 (6) (2022) 2309–2319.

[18] T.J. Levingstone, et al., Cell-free multi-layered collagen-based scaffolds demonstrate layer specific regeneration of functional osteochondral tissue in caprine joints, Biomaterials 87 (2016) 69–81.

[19] P.I. Mapp, D.A. Walsh, Mechanisms and targets of angiogenesis and nerve growth in osteoarthritis, Nat. Rev. Rheumatol. 8 (7) (2012) 390–398.

[20] A. Olsson, et al., Tasquinimod triggers an early change in the polarization of tumor associated macrophages in the tumor microenvironment, J Immunother Cancer 3 (2015) 53.

[21] J. Jin, J. Zhang, S. Bu, Tasquinimod efficacy and S100A9 expression in glucose-treated HREC cells, Int. Ophthalmol. 42 (2) (2022) 661–676.

[22] J. Zhang, et al., Osteoimmunity-regulating biomimetically hierarchical scaffold for augmented bone regeneration, Adv. Mater. 34 (36) (2022) e2202044.

[23] Z.U. Arif, et al., Recent advances in 3D-printed polylactide and polycaprolactone-based biomaterials for tissue engineering applications, Int. J. Biol. Macromol. 218 (2022) 930–968.

[24] Y. Wang, et al., Biomimetic glycopeptide hydrogel coated PCL/nHA scaffold for enhanced cranial bone regeneration via macrophage M2 polarization-induced osteo-immunomodulation, Biomaterials 285 (2022) 121538.

[25] B.J. Klotz, et al., Gelatin-methacryloyl hydrogels: towards biofabrication-based tissue repair, Trends Biotechnol. 34 (5) (2016) 394–407.

[26] W.L. Dai, et al., 3D bioprinting of heterogeneous constructs providing tissue-specific microenvironment based on host-guest modulated dynamic hydrogel bioink for osteochondral regeneration, Adv. Funct. Mater. 32 (23) (2022).

[27] L.W. Zhang, et al., Multileveled hierarchical hydrogel with continuous biophysical and biochemical gradients for enhanced repair of full-thickness osteochondral defect, Adv. Mater. 35 (19) (2023).

[28] H. Hu, et al., miR-23a-3p-abundant small extracellular vesicles released from Gelma/nanoclay hydrogel for cartilage regeneration, J. Extracell. Vesicles 9 (1) (2020) 1778883.

[29] Z. Qiao, et al., Bioinspired stratified electrowritten fiber-reinforced hydrogel constructs with layer-specific induction capacity for functional osteochondral regeneration, Biomaterials 266 (2021) 120385.

[30] D. Wu, et al., Exosomes Derived from bone mesenchymal stem Cells with the Stimulation of Fe_3O_4 Nanoparticles and static magnetic field enhance wound healing through Upregulated miR-21-5p, Int. J. Nanomed. 15 (2020) 7979–7993.

[31] Y. Han, et al., Biomimetic injectable hydrogel microspheres with enhanced lubrication and controllable drug release for the treatment of osteoarthritis, Bioact. Mater. 6 (10) (2021) 3596–3607.

[32] A. Irem Demir, et al., Comparison of 3 cell-free matrix scaffolds used to treat osteochondral lesions in a rabbit model, Am. J. Sports Med. 50 (5) (2022) 1399–1408.

[33] M. Rutgers, et al., Evaluation of histological scoring systems for tissue-engineered, repaired and osteoarthritic cartilage, Osteoarthritis Cartilage 18 (1) (2010) 12–23.

[34] C. Trapnell, et al., Differential gene and transcript expression analysis of RNA-seq experiments with TopHat and Cufflinks, Nat. Protoc. 7 (3) (2012) 562–578.

[35] U. Distler, et al., Label-free quantification in ion mobility-enhanced data-independent acquisition proteomics, Nat. Protoc. 11 (4) (2016) 795–812.

[36] C. Ding, et al., Regeneration of a goat femoral head using a tissue-specific, biphasic scaffold fabricated with CAD/CAM technology, Biomaterials 34 (28) (2013) 6706–6716.

[37] A.J. Engler, et al., Matrix elasticity directs stem cell lineage specification, Cell 126 (4) (2006) 677–689.

[38] X. Liu, X. Jin, P.X. Ma, Nanofibrous hollow microspheres self-assembled from star-shaped polymers as injectable cell carriers for knee repair, Nat. Mater. 10 (5) (2011) 398–406.

[39] J. Li, et al., Development and systematic characterization of GelMA/alginate/ PEGDMA/xanthan gum hydrogel bioink system for extrusion bioprinting, Biomaterials 293 (2023) 121969.

[40] Y.M. Pan, et al., Caveolin-1 is important for nitric oxide-mediated angiogenesis in fibrin gels with human umbilical vein endothelial cells, Acta Pharmacol. Sin. 27 (12) (2006) 1567–1574.

[41] N. Baker, J. Sohn, R.S. Tuan, Promotion of human mesenchymal stem cell osteogenesis by PI3-kinase/Akt signaling, and the influence of caveolin-1/ cholesterol homeostasis, Stem Cell Res. Ther. 6 (2015) 238.

[42] N. Bandara, et al., Molecular control of nitric oxide synthesis through eNOS and caveolin-1 interaction regulates osteogenic differentiation of adipose-derived stem cells by modulation of Wnt/beta-catenin signaling, Stem Cell Res. Ther. 7 (1) (2016) 182.

[43] N. Sears, et al., Fabrication of biomimetic bone grafts with multi-material 3D printing, Biofabrication 9 (2) (2017) 025020.

[44] J.Y. Liu, et al., Chitosan-based nanofibrous membrane unit with gradient compositional and structural features for mimicking calcified layer in osteochondral matrix, Int. J. Mol. Sci. 19 (8) (2018).

[45] Y. Huang, et al., Scaffold with natural calcified cartilage zone for osteochondral defect repair in minipigs, Am. J. Sports Med. 49 (7) (2021) 1883–1891.

[46] R.J. Lories, F.P. Luyten, The bone-cartilage unit in osteoarthritis, Nat. Rev. Rheumatol. 7 (1) (2011) 43–49.

[47] J.P. St-Pierre, et al., The incorporation of a zone of calcified cartilage improves the interfacial shear strength between in vitro-formed cartilage and the underlying substrate, Acta Biomater. 8 (4) (2012) 1603–1615.

[48] G.M. Cunniffe, et al., Tissue-specific extracellular matrix scaffolds for the regeneration of spatially complex musculoskeletal tissues, Biomaterials 188 (2019) 63–73.

[49] S.J. Jia, et al., Multilayered scaffold with a compact interfacial layer enhances osteochondral defect repair, ACS Appl. Mater. Interfaces 10 (24) (2018) 20296–20305.

[50] X. Ding, et al., Integrated trilayered silk fibroin scaffold for osteochondral differentiation of adipose-derived stem cells, ACS Appl. Mater. Interfaces 6 (19) (2014) 16696–16705.

[51] C. Zhai, et al., Repair of articular osteochondral defects using an integrated and biomimetic trilayered scaffold, Tissue Eng. 24 (21–22) (2018) 1680–1692.

[52] W. Liu, et al., Rapid continuous multimaterial extrusion bioprinting, Adv. Mater. 29 (3) (2017).

[53] A.L. Rutz, et al., A multimaterial bioink method for 3D printing tunable, cell-compatible hydrogels, Adv. Mater. 27 (9) (2015) 1607–1614.

[54] C. Wang, et al., 3D printing of bone tissue engineering scaffolds, Bioact. Mater. 5 (1) (2020) 82–91.

[55] A. Ovsianikov, A. Khademhosseini, V. Mironov, The synergy of scaffold-based and scaffold-free tissue engineering strategies, Trends Biotechnol. 36 (4) (2018) 348–357.

[56] J. Lee, et al., Directed regeneration of osteochondral tissue by hierarchical assembly of spatially organized composite spheroids, Adv. Sci. 9 (3) (2022) e2103525.

[57] Q.Y. Huang, et al., A review of the role of cav-1 in neuropathology and neural recovery after ischemic stroke, J. Neuroinflammation 15 (2018).

[58] Y.M. Pan, et al., Caveolin-1 is important for nitric oxide-mediated angiogenesis in fibrin gels with human umbilical vein endothelial cells, Acta Pharmacol. Sin. 27 (12) (2006) 1567–1574.

[59] C. Scotti, et al., Stem cells for cartilage regeneration: a roadmap to the clinic, Stem Cell. Int. 2018 (2018) 7348560.